

This is a preprint of the following article, which is available from <http://mdolab.engin.umich.edu>
Yingqian Liao, Nitin Garg, Joaquim R. R. A. Martins, and Yin Lu Young. Viscous Fluid Structure Interaction Response of Composite Hydrofoils. *Composite Structures*, 212 (2019) 571-585.

The published article may differ from this preprint, and is available by following the DOI: <https://doi.org/10.1016/j.compstruct.2019.01.043>.

Viscous Fluid Structure Interaction Response of Composite Hydrofoils

Yingqian Liao¹, Nitin Garg¹, Joaquim R. R. A. Martins², Yin Lu Young¹

¹*Department of Naval Architecture and Marine Engineering, University of Michigan, Ann Arbor, MI, 48109*

²*Department of Aerospace Engineering, University of Michigan, Ann Arbor, MI, 48109*

Abstract

Composite materials are increasingly used in hydrodynamic lifting surfaces due to their higher specific strength and favorable fatigue properties. A set of parametric studies are performed to investigate the influence of fiber orientation on the vibration characteristics and load-dependent bend-twist coupled behavior of composite hydrofoils in viscous flow. A 3-D Reynolds-averaged Navier–Stokes (RANS) solver is coupled with a 3-D finite-element method (FEM) to predict the fluid-structure response of cantilevered composite hydrofoils made of unidirectional carbon fiber reinforced polymer (CFRP). Fiber orientation changes the modal characteristics of composite hydrofoils, as well as the hydroelastic response. The bending-up and nose-down material bend-twist coupling leads to lower hydrodynamic load coefficients with increasing flow speed, as well as delayed separation, stall, and static divergence. The opposite trend is observed when the fiber orientation results in a bending-up and nose-up material bend-twist coupling. Material failure index contours show that the fiber orientation affects the location of failure. These parametric studies provide guidance for future design and optimization of composite hydrodynamic lifting surfaces.

1 Introduction

According to the Review of Maritime Transport of United Nations Conference on Trade and Development [1], maritime transport still contributes to more than 80% of the total world trade. Thus, improving the marine transport efficiency is critical for global sustainability, as well as for economic worldwide growth. Additionally, increasingly stringent energy efficiency requirements for ships [2] encourages researchers and

ship builders to look for ways to increase the efficiency of maritime transport. Two promising ways to address this are to use new materials for the hull and propulsor, and to use more sophisticated design methodologies, such as multidisciplinary design optimization [3–13].

Traditionally, marine propellers are made of metallic alloys such as nickel aluminum bronze (NAB) [9, 14, 15]. NAB has the advantages of high-stiffness, anti-biofouling, good corrosion resistance in salt water, and high resistance to cavitation erosion. Another reason to use NAB is that a great deal of experience and data have been accumulated on its use and properties. However, the performance of metallic structures is now reaching its limits. Even a well-designed metallic propeller undergoes a noteworthy efficiency loss when operating at off-design conditions [9].

Thanks to recent advances in fiber-reinforced materials, as well as the development of reliable high-quality manufacturing processes, we can now take advantage of new composite materials to improve the efficiency and reliability of marine lifting surfaces. Composite materials have already been widely used in aerospace and wind energy applications. Carbon fiber reinforced polymers (CFRPs) have become one of the main materials in aircraft since their introduction in 1970s [16, 17]. Aeroelastic tailoring via composite material layup has shown to be capable of increasing the critical divergence and flutter speed [18]. A more recent work by Brooks et al. [19] showed a reduction in fuel burn and wing weight when using numerical optimization to design high-aspect ratio wings with composites. Hayat and Ha [20] showed that adding ply-thickness unbalance to ply-angle and ply-material unbalances in wind turbine design reduced the fatigue load and reduced the pitch-actuator duty. Compared to aerospace designs, the use of composites in marine applications is more challenging due to the much higher fluid density of water, and the harsher marine environment. Many composite marine hydrodynamic lifting bodies are based on cantilevered structures, including propellers, turbine blades, hydrofoils, keels, rudders, and different control surfaces [9, 21]. Composite materials are preferred because of their higher strength-to-weight ratio, which allows for weight reduction while satisfying the strength requirements, higher damping for reducing vibration and mitigating noise [22, 23], and self-adaptability through strategic tailoring of material bend-twist coupling behavior. Isotropic cantilevered structures experience flow-induced bend-twist coupling when the center of lift does not coincide with the elastic axis location. In addition to flow-induced bend-twist coupling, material anisotropy can introduce additional bend-twist coupling that can be used to passively tailor the hydroelastic response of the composite structures to improve performance [9–11]. Composite materials also have disadvantages, such as complex failure mechanisms, requirements of advanced manufacturing techniques, and impact damage followed by water absorption, but we can avoid the relevant negative consequences by enforcing the appropriate constraints in multidisciplinary design optimization.

Various numerical works have been conducted to investigate the hydroelastic behaviors of marine lifting surfaces and optimize the designs. Lin [24] first conducted a finite-element analysis on a composite propeller blade to estimate its performance. Recently, a 3-D boundary element method (BEM) has been coupled with a 3-D finite element method (FEM) for the fluid-structure interaction analysis of adaptive composite marine propellers [10, 11, 25–27]. The 3-D BEM-FEM coupled model is able

to predict the hydroelastic performance, cavitation or ventilation patterns, stresses, deformations, vibration characteristics, and potential material failure mechanisms of composite marine propellers in spatially varying flow. These numerical works showed that tailoring of anisotropic properties of composites can increase the overall efficiency and delay cavitation inception of marine propellers compared to metallic counterparts when operating in a spatially varying wake [10, 11, 25–28]. Plucinski et al. [28] used the same coupled 3-D BEM-FEM method with genetic algorithms to optimize a multi-layered composite propeller by minimizing the gap between the optimal operating angles and the deformed pitched angles over several flow conditions. To find an optimal fiber orientation for reducing the total fuel consumption, Blasques et al. [8] used a gradient-free optimization algorithm on a BEM-FEM coupled model. They found that the curved fiber path was more efficient than the straight path. Similarly, experimental work showed that passive de-pitching action induced by material bend-twist coupling reduced the tip loading and therefore delayed the cavitation inception [9, 29]. Young et al. [15] provided experimental measurement and numerical analysis of the performance of three composite hydrofoils with different orientation for the structural CFRP layers, and compared their performance to a rigid stainless steel hydrofoil. They concluded that the material bend-twist coupling had a significant effect on the mode shapes and modal frequencies, and modified the hydrodynamic forces, the stall boundary, and the static divergence speed.

Most of the previous work on composite hydrodynamic lifting surfaces used low-fidelity tools, such as the BEM method, which assumes inviscid and irrotational flow. Low-fidelity tools are favored due to their low computational cost, but they cannot capture viscous effects such as separation and stall. Considering viscous effects is critical to yield a reliable estimation of flow separation and resultant change in pressure distribution, lift, drag, moment, cavitation inception speed, bend-twist deformations, vibrations, noise, and material failure. Hence, high-fidelity simulations are required to capture viscous fluid-structure interaction effects and accurately predict the performance of composite marine structures.

Garg et al. [30] developed a framework for high-fidelity design optimization of hydrofoils that couples a Reynolds-averaged Navier–Stokes (RANS) solver to a structural finite element method (FEM) solver. This framework was originally developed for the design of aircraft wings by Kenway et al. [31, 32] and is called MACH (multidisciplinary design optimization of aircraft configurations with high-fidelity). It uses a gradient-based approach with an efficient gradient computation that enables optimization with respect to large numbers of shape and structural sizing variables. Garg et al. [30] performed the shape optimization of metal hydrofoils considering cavitation and strength constraints and the optimized design was validated by experiments [33].

The eventual goal of our work is to design adaptive marine lifting surfaces that take advantage of the tailoring of anisotropic composites using MACH. However, prior to design, it is crucial that we understand the basic physics that govern the response of composite hydrodynamic lifting bodies, including its steady-state hydroelastic response and vibration characteristics. In addition, although MACH has already been used to perform the design optimization of composite aircraft wings [19, 34], the wing structures were modeled with shell finite elements, while we require solid composite finite elements

for modeling hydrofoils because of the thicker sections required to withstand the higher loads caused by the higher fluid density.

To address the needs and motivation stated above, the objectives of this work are to (1) develop and verify a high-fidelity hydrostructural solver for the analysis of the hydroelastic performance and the susceptibility to material failure of composite hydrofoils in viscous flow, and to predict the relevant free vibration characteristics, and (2) improve the understanding of load-dependent bend-twist coupling effects on the hydroelastic performance of composite hydrofoils in viscous flow through numerical simulations.

2 Methodology

In this work, we implemented an approach to model composite structures with orthotropic materials using solid elements in MACH. We then used the MACH framework to simulate the hydroelastic response of composite hydrofoils with different unidirectional CFRP orientations and to analyze the influence of the fiber orientation on the response. The geometry of the hydrofoil is generated by pyGeo, which is a CAD-free python module tool using free-form deformation volume approach [35]. We import the geometry into ICEM-CFD to generate surface mesh, and use pyHyp to extrude the surface mesh into a hyperbolic volume mesh.

The computational fluid dynamics solver in MACH is ADflow, a second order finite-volume solver. ADflow solves the Euler, laminar Navier–Stokes, and RANS equations on multiblock or overset meshes. Mader et al. [36] and Lyu et al. [37] have enabled ADflow to compute sensitivities with respect to a large number of variables by implementing an adjoint method, which is critical for gradient-based optimization. In the current work, the Spalart–Allmaras (SA) [38] turbulence model is used in the RANS equations. For computational efficiency, we start solving the equations by diagonalized alternating direction implicit and approximate Newton–Krylov algorithms, and then switch to Newton–Krylov solver after the residual has reduced below a given tolerance.

The structural solver used in the MACH framework is the Toolkit for the Analysis of Composite Structures (TACS) [39]. TACS is a parallel, general 3-D FEM solver for structural analysis that can also compute gradients using an adjoint method. TACS specializes in solving ill-conditioned thin-shell structures problems, which are common in aircraft design. However, a solid interior structure is required for hydrodynamic lifting bodies due to the higher fluid loading. Therefore, we implemented solid orthotropic elements in TACS, more specifically, an 8-node brick element (CHEXA8) to simulate the response of composite structures using the solid element [40].

We model the composite hydrofoils using the orthotropic material properties, which require nine independent constants for their stress-strain relationship. When the fibers are not aligned with global coordinates (Figure 1), a transformation of stress and strain is required. The final constitutive equations for orthotropic elements in global coordinates can be found in Appendix A.

The CFD and the structural solvers described above are coupled to predict the hydrodynamic loads, solid stresses, and deformations for given flow conditions. The

hydrodynamic loads (pressure and shear stress distributions) computed by ADflow are transferred to the structural solver using the method of virtual work [32, 41]. The displacements from the structural solution are extrapolated to the CFD surface mesh through rigid links [32, 41], and are propagated to the volume mesh using a mesh deformation algorithm [42].

3 Verification

The CFD solver has already been validated in the work of Garg et al. [30, 43]. Hence, the objective of this section is to verify TACS for composite structures. We verify the new solid orthotropic elements in TACS by comparing the predicted modal analysis results and static pressure deformation results with those obtained using the commercial solver ABAQUS with 8-noded brick element (C3D8). In the second part, we perform FEM mesh and CFD mesh convergence studies to determine the appropriate mesh size to be used.

3.1 Free vibration response and static deformation comparison

To verify the TACS computations, we use the plate model made of unidirectional CFRP, as shown in Figure 1, where the plate is cantilevered at the left side is fixed. The material properties for the composite plate are listed in Table 1, which are the same as the values used in the study by Kramer et al. [21]. The fiber orientation angle θ_f is defined relative to the spanwise axis and is positive towards the plate leading edge, as shown in Figure 1 by the axis labeled ‘2’. Positive values of θ_f indicate fibers that are rotated forward relative to the spanwise axis, while negative values indicate fibers are rotated backward.

Table 1: Composite plate material properties and water properties used to predict the in-air and in-water natural frequencies shown in Figure 2

Symbol	Description	Value	Units
ρ_s	Solid density	1500	Kg/m ³
E_2	Young’s modulus	171.42	GPa
E_1, E_3	Young’s modulus	9.08	GPa
G_{12}, G_{23}	Shear modulus	5.29	GPa
G_{13}	Shear modulus	0.28	GPa
ν_{12}, ν_{23}	Poisson’s ratio	0.32	–
ν_{13}	Poisson’s ratio	0.29	–
ρ_f	Fluid density	998	Kg/m ³
K_f	Fluid bulk modulus	2.2	GPa

In Table 2, we see that the first two in-air natural frequencies of the composite plate with $\theta_f = -30^\circ$ using four different meshes show good agreement between the two FEM solvers. The fine mesh listed in Table 2 is used for modal analysis for various θ_f in

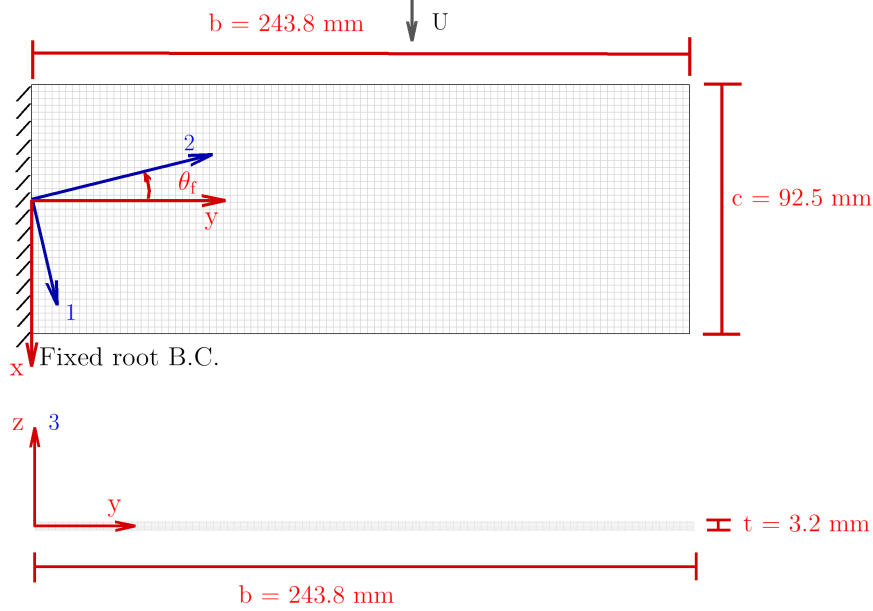


Figure 1: Cantilevered plate (with the fine mesh and dimensions) used for the verification study. The fixed edge is on the left. Red axes represent global coordinates, while dark blue axes represent the local coordinate with the fibers aligned along the 2-direction, which is at a positive θ_f relative to the spanwise axis.

Figure 2. The results shown on the left side of Figure 2 demonstrate good agreement between TACS and ABAQUS for the first four predicted in-air natural frequencies. The maximum discrepancy in frequencies for the first in-air mode is 0.9% for $\theta_f = 90^\circ$ (i.e, fibers aligned with the streamwise direction), while the maximum discrepancy is 0.8% for the fourth in-air mode.

Table 2: Verification of the in-air natural frequencies for various structural mesh resolutions for a cantilevered plate with $\theta_f = -30^\circ$.

Mesh	n_x	n_y	n_z	Mode 1 [Hz]		Mode 2 [Hz]	
				ABAQUS	TACS	ABAQUS	TACS
Coarse	48	18	5	49.1	49.4	240.4	238.7
Medium	72	27	7	45.5	45.7	226.9	226.1
Fine	96	36	9	44.1	44.2	221.6	221.1
Finest	120	48	12	43.5	43.5	218.8	218.5

Due to the added mass effect in water, the vibration characteristics can change substantially. The right side of Figure 2 shows the first four predicted in-water natural frequencies obtained using ABAQUS. Acoustic elements are used to simulate the water, and non-reflecting boundary conditions are applied at the edges of the acoustic fluid domain. The assumed properties for water are listed in Table 1. As shown in Figure 2, the in-water frequencies of the plate are much lower than the corresponding in-air frequencies. This is consistent with findings from previous numerical and experimental

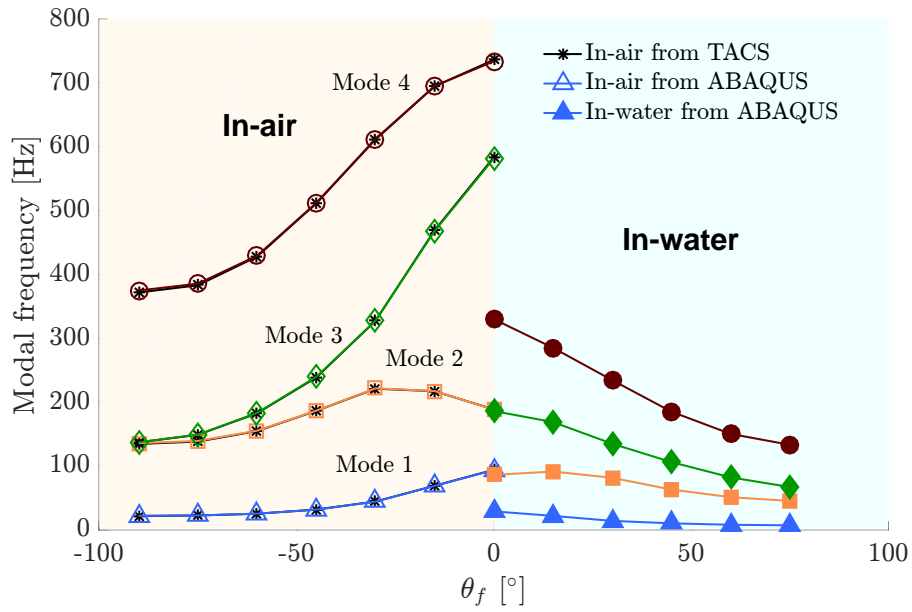


Figure 2: Comparison of the first four predicted in-air natural frequencies (left half plane) from ABAQUS (open symbols) and TACS (star symbols), and comparison of the first four in-water natural frequencies (right half plane, calculated from ABAQUS) for the plate of Figure 1 with varying fiber orientation angle θ_f . Note that the natural frequencies are much lower in water due to added mass effects.

work [9, 15, 21, 44, 45]. The predicted in-air and in-water mode shapes are shown in Figure 3. The contours represent the scaled displacement amplitude, which is the magnitude of the scaled displacement vector. Since the displacement amplitude of the modal analysis results is not physical, the contour scales are for visualization of the mode shape only. As shown in Figure 3, the first mode is primarily bending, while the second mode can be bending or twisting, depending on the fiber orientation. Bending motion is accompanied by a large volume of displaced water, which leads to higher fluid inertial resistance, causing a greater reduction in natural frequencies when operating in water. Since the effect of the surrounding fluid is different for bending-dominated versus twisting-dominated modes, the order of the modes can switch with fiber orientation, and can be different than that in air. Nevertheless, for the plate shown in Figure 1, the in-air and in-water mode shapes are similar, and no mode switching is observed.

To further verify TACs, comparisons of the predicted tip bending δ_{tip} and tip twist θ_{tip} deformations obtained using TACS and ABAQUS for the plate are shown in Figure 4. The results correspond to the plate subject to a uniform pressure of 443.5 Pa. Good agreement is observed between these two FEM solvers. The maximum discrepancy of δ_{tip} is 1.87% for $\theta_f = 90^\circ$. The maximum difference of θ_{tip} is less than 0.0003° for $\theta_f = 90^\circ$.

3.2 Mesh convergence study for a composite hydrofoil

The previous section verified the new solid composite element formulation in TACS. The objective of this section is to perform a convergence study to determine the optimal mesh for the composite hydrofoil to be used to produce our results. We first present the geometry and material properties of the hydrofoil, followed by FEM and CFD mesh convergence studies.

3.2.1 Hydrofoil model

For a geometry that is more realistic than a simple cantilevered plate, we use a canonical linearly tapered hydrofoil composed of unidirectional CFRP with no built-in twist to study the hydroelastic response. The cross section is a modified NACA 0009 with a thicker trailing edge than the original section [46]. The hydrofoil has a span of $2b = 0.6$ m, a mean chord of $c = 0.09$ m, and a taper ratio of 0.5, as shown in Figure 5. The resulting aspect ratio of the hydrofoil is 6.67. The bottom plot in Figure 5 shows the structural mesh, which has 121,800 elements. Fixed boundary conditions are enforced at the root. The angle θ_f is defined relative to the spanwise axis and is positive towards the foil leading edge. Unidirectional CFRP is used throughout in these studies; its material properties are listed in Table 3. All computations in the mesh convergence study are performed with $\theta_f = -30^\circ$ unless otherwise stated. All hydrostructural computations are performed at a Reynolds number of 10^6 unless otherwise stated.

3.2.2 FEM mesh convergence study

The convergence study results for the predicted in-air natural frequencies are shown in Table 4. The difference in the third mode frequency between TACS and ABAQUS

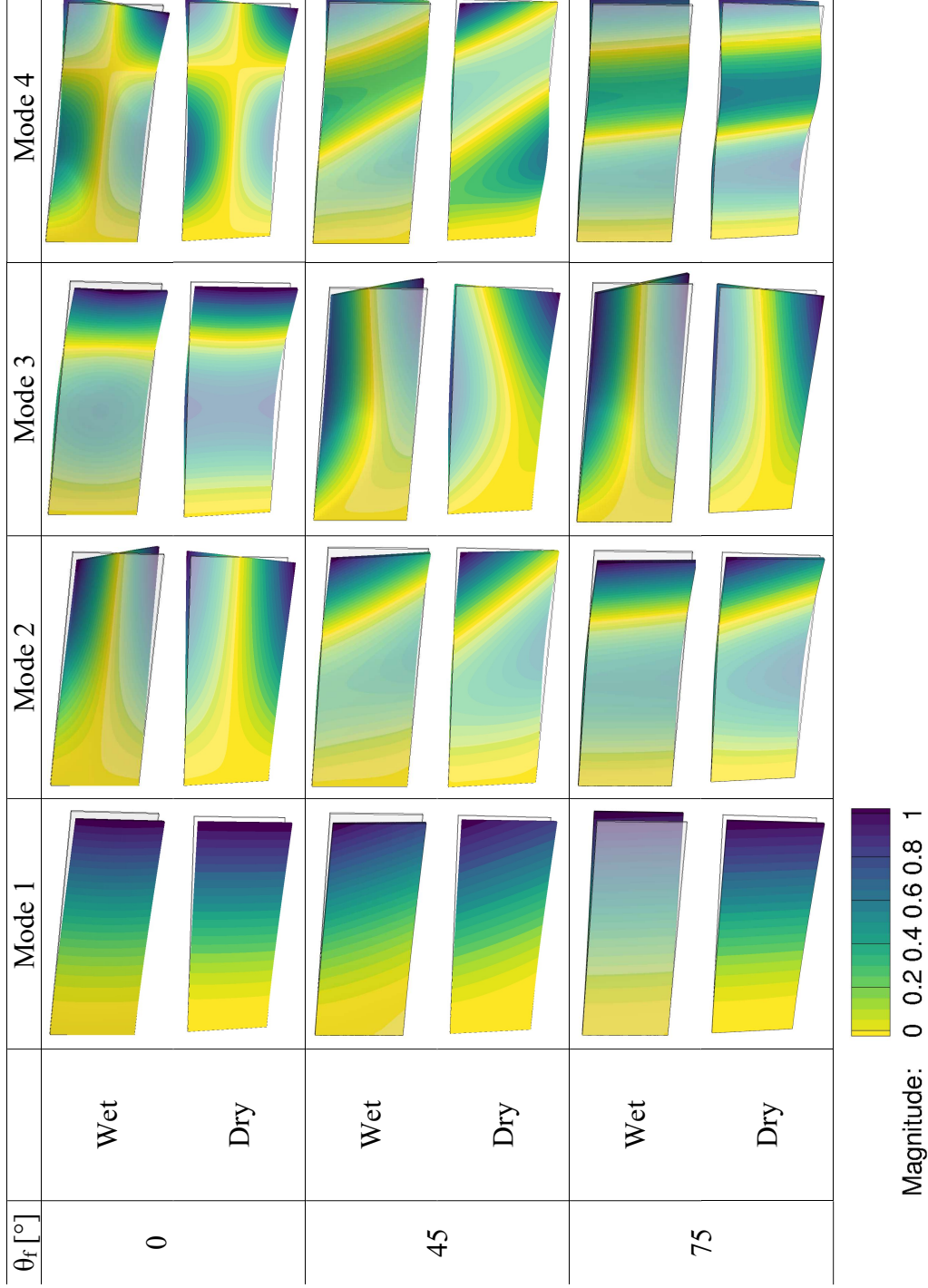


Figure 3: Comparison of the first four predicted in-air mode shapes and first four predicted in-water mode shapes of a cantilevered foil for unidirectional fiber orientations $\theta_f = 0^\circ, 45^\circ, 75^\circ$ obtained using ABAQUS. The contours represent the scaled displacement amplitude. Note that the contour legend only shows a normalized range and does not imply the actual displacement magnitude.

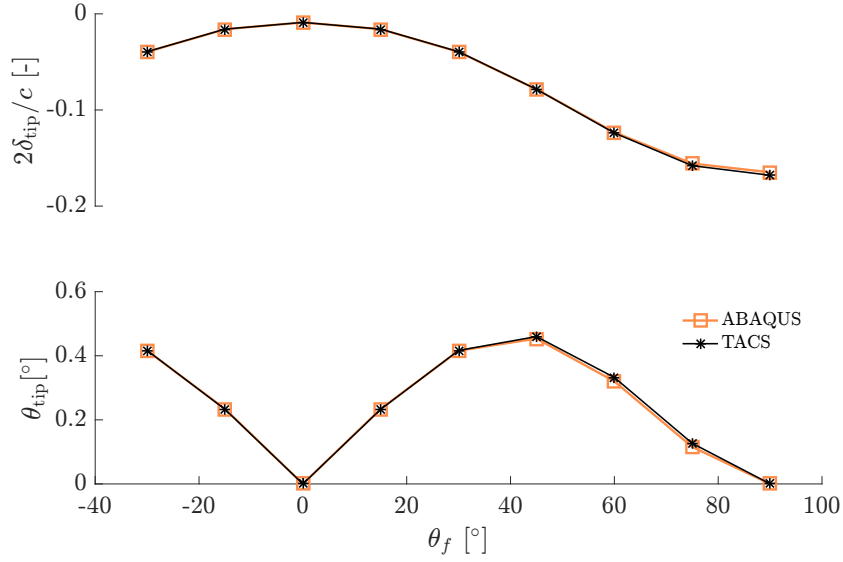


Figure 4: Comparison of the predicted tip bending and tip twist deformations from ABAQUS and TACS for the composite plate. The deflections are measured at the mid-chord at the tip.

Table 3: CFRP material properties.

Symbol	Description	Value	Units
ρ_s	Solid density	1540	Kg/m ³
E_1	Young's modulus	13.40	GPa
E_2	Young's modulus	117.80	GPa
E_3	Young's modulus	9.40	GPa
G_{12}, G_{23}	Shear modulus	3.90	GPa
G_{13}	Shear modulus	3.30	GPa
ν_{12}, ν_{23}	Poisson's ratio	0.25	–
ν_{13}	Poisson's ratio	0.45	–
$X_T, Z_T/ X_C, Z_C$	Transverse tensile/compressive strength	50/250	MPa
S_{12}, S_{23}	Shear strength	70	MPa
S_{13}	Shear strength	26	MPa

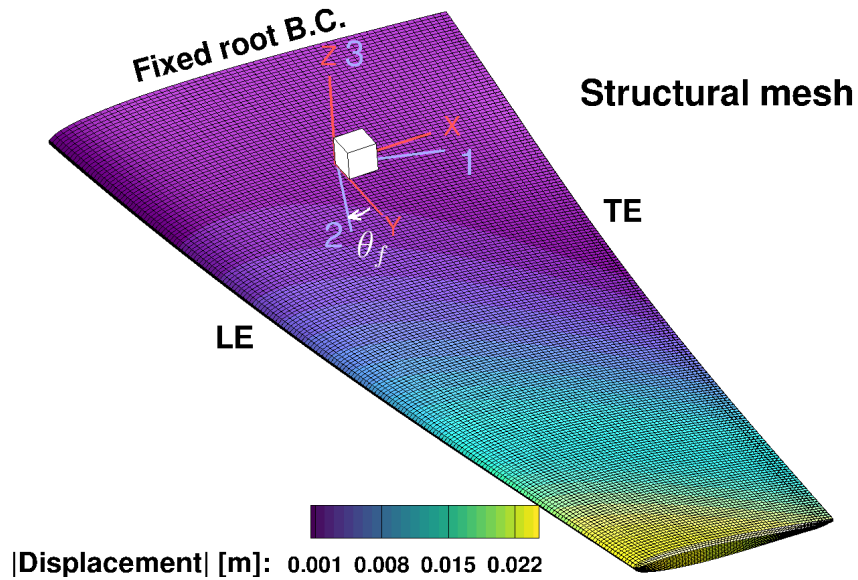
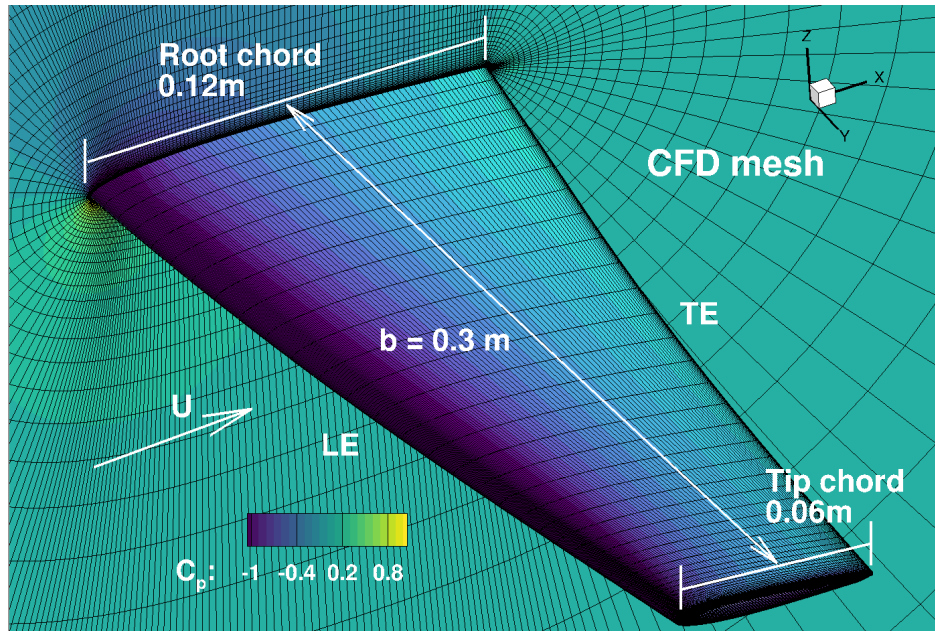


Figure 5: Hydrostructural analysis of the CFRP hydrofoil with $\theta_f = -30^\circ$ at $Re = 10^6$ and $\alpha = 6^\circ$. Top: CFD mesh for the cantilevered NACA 0009 hydrofoil with 1,073,520 cells. Bottom: Structural mesh and displacement magnitude contours on the deformed geometry using with 121,800 8-node linear brick elements.

is only 0.99%. Increasing the mesh resolution from medium to fine only changes the third in-air natural frequency by 0.08% in the TACS analysis.

In addition to the in-air natural frequencies predicted using TACS, we present the structural mesh convergence study by the hydrostructural analysis of the composite hydrofoil with $\theta_f = -30^\circ$ and angle of attack of 2° . The angle of attack (α) is defined as the angle between the chord line at the root of the hydrofoil and the free stream, and is positive when the leading edge is up. A CFD mesh with 4,924,800 cells ($y_{\max}^+ = 7.5$) is used in ADflow for all cases. The resultant lift coefficient C_L , drag coefficient C_D , pitch moment coefficient C_M , non-dimensionalized tip bending deformation $2\delta_{\text{tip}}/c$, and tip twisting θ_{tip} are summarized in Table 5. C_M is defined about mid chord at the root and positive nose up. Table 5 shows that the 121,800 element mesh yields a good balance between computational efficiency and the accurate hydrostructural response prediction.

Table 4: FEM mesh convergence study for the in-air natural frequencies computed using 8-node linear brick elements: C3D8 in ABAQUS and CHEXA8 in TACS.

Mesh	Elements	n_y	n_x	n_z	Mode 1 [Hz]		Mode 2 [Hz]		Mode 3 [Hz]	
					ABAQUS	TACS	ABAQUS	TACS	ABAQUS	TACS
Coarse	73,350	163	50	9	97.5	97.7	412.4	412.7	718.6	710.0
Medium	121,800	203	60	10	97.2	97.3	410.8	411.0	715.8	708.7
Fine	187,100	243	70	11	97.0	97.1	409.9	410.1	714.0	708.1
Finest	271,680	283	80	12	96.9	97.0	409.3	409.4	712.6	707.6

Table 5: FEM mesh convergence study for the hydrodynamic coefficients, tip bending, and tip twist obtained using TACS coupled with ADflow, for which a mesh of 4,924,800 cells is used.

Mesh	Elements	C_L	C_D	C_M	$2\delta_{\text{tip}}/c$	$\theta_{\text{tip}} [^\circ]$
Coarse	73,350	0.268	0.0131	0.0635	0.199	2.08
Medium	121,800	0.268	0.0131	0.0637	0.201	2.10
Fine	187,100	0.269	0.0131	0.0635	0.203	2.03
Finest	271,680	0.270	0.0131	0.0639	0.203	2.19

3.2.3 CFD mesh convergence study

The CFD convergence study is completed with five different mesh sizes, as listed in Table 6. All these results correspond to the same hydrofoil as above, at the same flow condition ($Re = 10^6$ and $\alpha = 2^\circ$). The same structural mesh with 187,100 elements is used in TACS for this study. The results are summarized in Table 6. The difference between experimental values marked in Figure 6 and the Richardson extrapolation of the numerical results is partly due to the difference in actual material used in the experiment versus the material assumed in this study. Since our goal is to demonstrate the capability of the MACH framework to perform coupled hydrostructural analysis with

composite solid elements, we select the L3 CFD mesh shown in Table 6 to generate the subsequent results for a good balance between accuracy and computational efficiency. This mesh has $y_{\max}^+ = 10$, which is small enough such that no wall function is needed.

Table 6: CFD mesh convergence study of the hydrodynamic coefficients with a constant FEM mesh of 187,100 elements. The L3 mesh is selected for subsequent analysis considering the balance between accuracy and computational cost.

Mesh	Cells	C_L	C_D
L1	8,588,160	0.268	0.0126
L2	4,924,800	0.269	0.0131
L3	1,073,520	0.268	0.0158
L4	615,600	0.263	0.0206
L5	76,950	0.217	0.0648

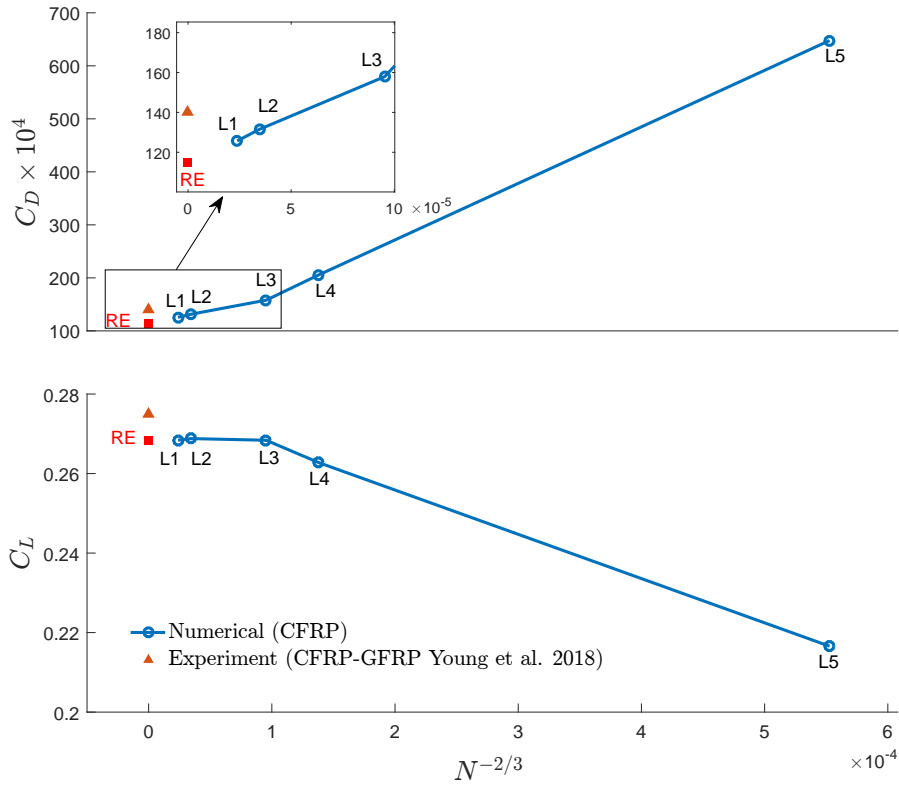


Figure 6: CFD mesh convergence study for hydrostructural analysis using same FEM mesh with 187,100 elements and CFD meshes listed in Table 6. Results computed with Richardson extrapolation (RE) are shown as red filled symbols.

4 Results

In the previous section, we verified the convergence characteristics of the FEM and CFD solvers. We now turn to our main goal, which is to investigate the influence of fiber orientation on the hydroelastic response of the composite hydrofoils. We first show results for modal and hydrostructural analyses, and then discuss the influence of the fiber orientation on the hydroelastic performance. Finally, we discuss the influence of fiber orientation on the susceptibility to static divergence and to material matrix/compressive cracking and delamination in tension/compression failures.

4.1 Free vibration response

Understanding how the free vibration response varies with fiber orientation is important because it sheds light on the stiffness and the material bend-twist coupling behavior, which in turn affects the hydroelastic performance. In addition, it is important to understand how the natural frequencies change with fiber orientation to avoid resonance and other hydroelastic instability issues. Based on the FEM mesh convergence study of Section 3.2.2, we selected the 121,800 element mesh for all the TACS computations.

The predicted in-air natural frequencies for θ_f ranging from -90° to 90° are plotted in Figure 7 for both TACS and ABAQUS computations. The results from the two solvers show excellent agreement for all investigated θ_f .

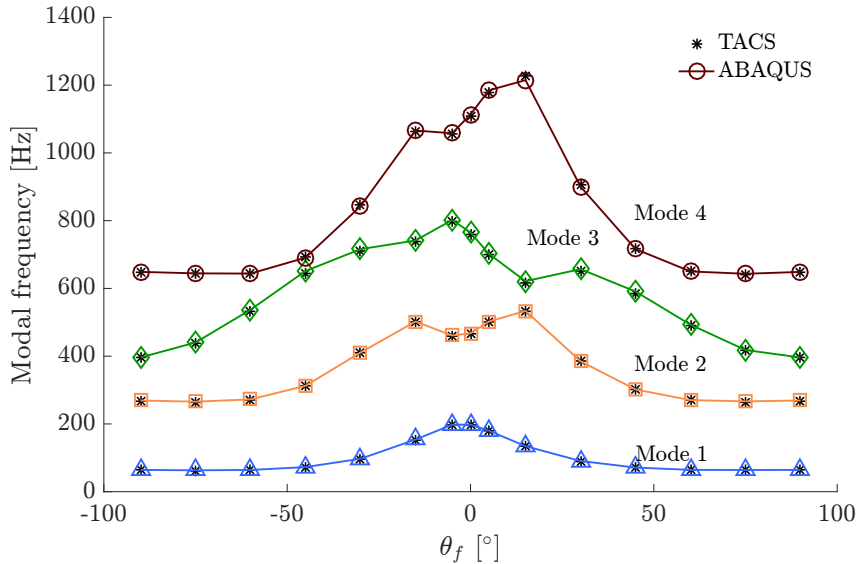


Figure 7: First four in-air natural frequencies computed with ABAQUS and TACS for the cantilevered CFRP hydrofoil (shown in Figure 5) for a range of θ_f .

The predicted mode shapes from TACS are shown in Figure 8, where the contours represent the scaled displacement amplitude, and a similar plot for ABAQUS computations is included in Appendix B. The mode shapes from TACS and ABAQUS are almost identical. The mode shapes are important because the displacements govern the

fluid added mass, which has a significant impact on the in-water natural frequencies, as illustrated earlier in Figure 2.

In Figure 8 we can see that the first modes for all θ_f are bending-dominated because of the high aspect ratio of the hydrofoil. When the fibers are oriented away from the spanwise axis (either forward or backward), the bending rigidity is decreased, which is evident through the decrease of the first mode frequency with increasing θ_f in Figure 7. Similarly, while the second mode for $\theta_f = 0^\circ$ is primarily twisting, a combination of bending and twisting can be observed from the mode shapes for $\theta_f \neq 0^\circ$. As $|\theta_f|$ increases, the bending rigidity weakens to an extent where the second mode becomes the second bending mode and the third mode becomes the first twisting mode. In addition, the twist direction is opposite for $\theta_f > 0^\circ$ and $\theta_f < 0^\circ$, which has direct implications on the hydroelastic response, as we will see later. For the fourth mode, when $|\theta_f| > 30^\circ$, an in-plane (or lead-lag) mode develops, while second order coupled bending and twisting is observed for $|\theta_f| < 30^\circ$.

Overall, the results in Figures 7 and 8 demonstrate that the natural frequencies and mode shapes vary significantly with the fiber orientation, suggesting the possibility of tailoring the fiber orientation to avoid resonant vibrations and tailoring the bend-twist coupling response to improve the hydroelastic performance.

4.2 Hydrostructural response

As suggested earlier, tailoring the material bend-twist coupling by varying the fiber orientation has a direct impact on the hydroelastic displacement of composite hydrofoils. This in turn impacts hydrodynamic loads, drag, lift, flow separation and stall boundaries, critical static divergence speed, and material failure location.

We compare the results for three different hydrofoils, each analyzed for two different cases in Figure 9. The three hydrofoils have an identical unloaded geometry and consist of two CFRP hydrofoils with fibers swept backward ($\theta_f = -30^\circ$) and fibers swept forward ($\theta_f = +30^\circ$), and a solid stainless steel hydrofoil. The two conditions are a fixed angle of attack ($\alpha = 10^\circ$), shown on the left of half of Figure 9, and a fixed lift coefficient ($C_L = 0.75$), shown on the right. For each of these cases, Figure 9 shows the initial and deformed geometries, streamlines, pressure coefficient contours on the foil suction side, as well as tip vortex streamlines and spanwise lift distributions for two flow conditions. The elliptical lift distributions are shown as a reference, since they represent the theoretical ideal distribution with minimum induced drag.

From Figure 9, we can see that while the stainless hydrofoil exhibits negligible deformation, the CFRP hydrofoils are much more flexible. Changing the fiber orientation effectively moves the elastic axis of hydrofoil, inducing bend-twist coupling. The CFRP hydrofoil with $\theta_f = -30^\circ$ yields bending-up and nose-up bend-twist coupling, while the one with $\theta_f = +30^\circ$ yields bending-up and nose-down bend-twist coupling. Hence, at $\alpha = 10^\circ$, the hydrofoil with $\theta_f = -30^\circ$ has a higher lift coefficient than the stainless steel and $\theta_f = +30^\circ$ hydrofoils, because of the higher overall effective angle of attack caused by the nose-up twist. Excessive effective angle of attack leads to flow separation and reduction in lift when stall develops. As shown on the left plots in Figure 9, when $\alpha = 10^\circ$ for the for $\theta_f = -30^\circ$ hydrofoil, the effective angle of attack is so large that

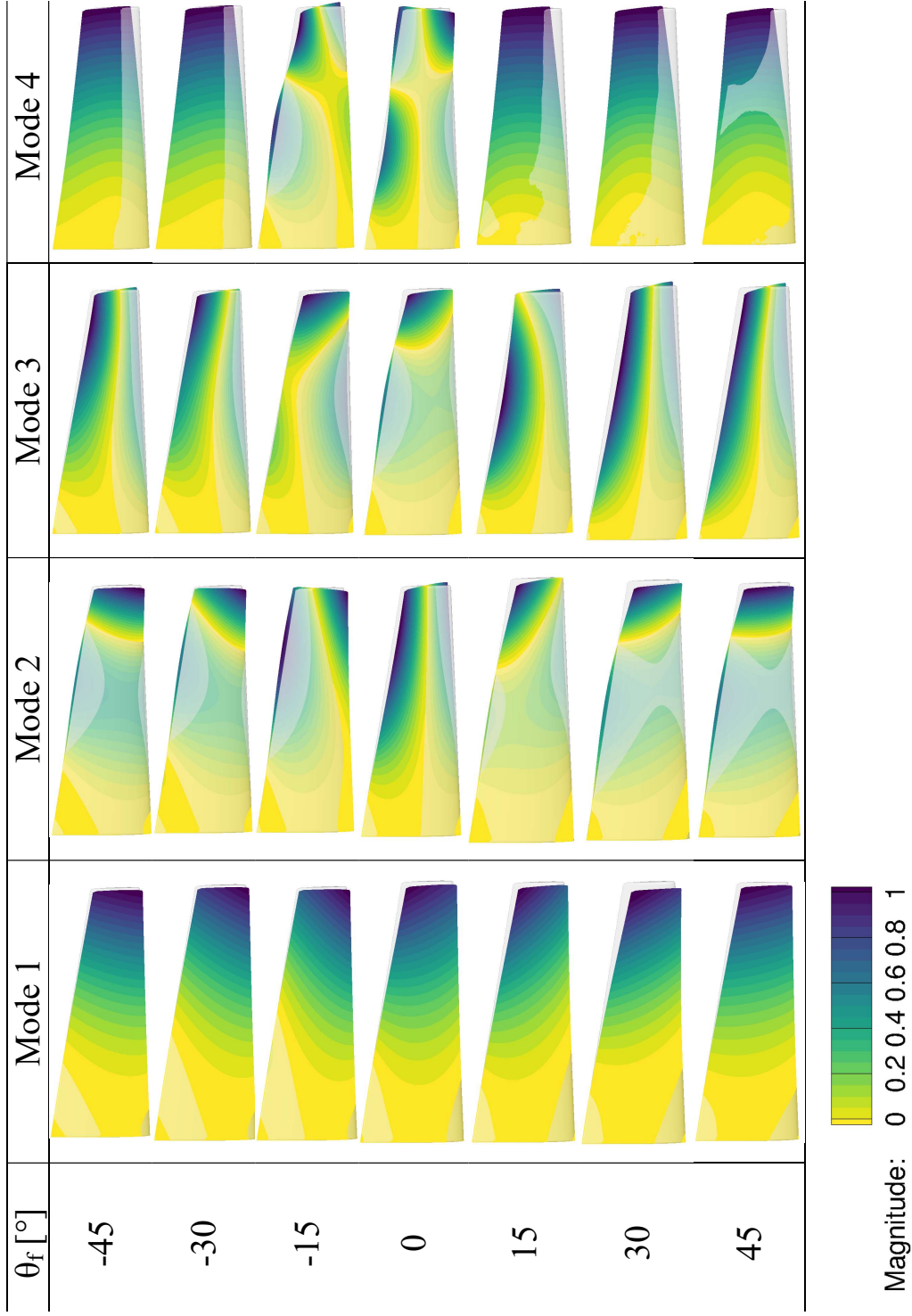


Figure 8: First four predicted in-air mode shapes for a range of θ_f obtained using TACS. The color map represent the scaled displacement amplitude. Note that the contour legend only shows a normalized range and does not imply the actual displacement magnitude. The predicted mode shapes using TACS agree well with those obtained using ABAQUS (shown in Appendix B).

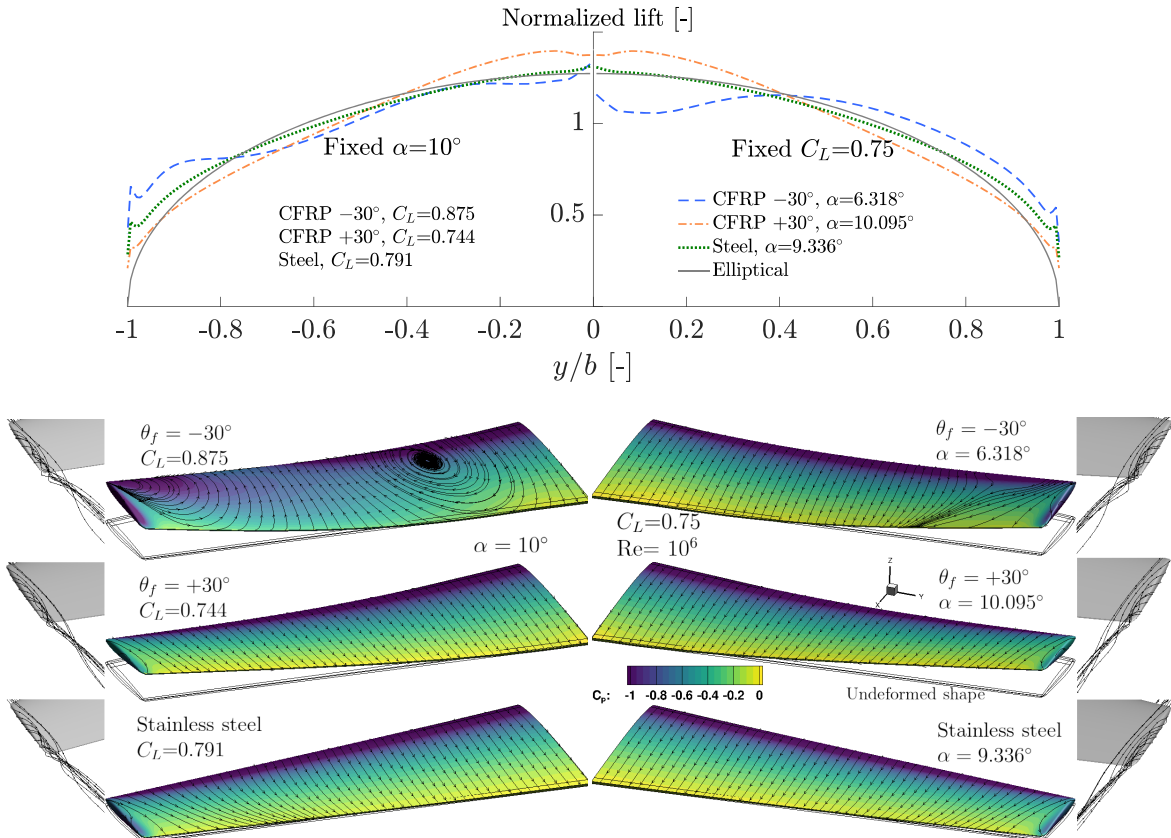


Figure 9: Deformed shapes, flow streamlines, pressure coefficient contours, tip vortex, and normalized sectional lift distributions for the CFRP hydrofoils with $\theta_f = -30^\circ$ (top) and $\theta_f = 30^\circ$ (middle) and the stainless steel (bottom) hydrofoil. The initial undeformed shape (black wireframe) and ideal elliptical lift distribution are provided as reference here. The left plots show results for $\alpha = 10^\circ$. The right plots show results for $C_L = 0.75$.

the flow is nearly fully separated. On the other hand the flow stays mostly attached for the $\theta_f = +30^\circ$ and stainless steel hydrofoils. Flow separation affects the pressure distribution, and thus changes the spanwise lift distribution significantly, as shown on the top of Figure 9.

Lifting surfaces are usually required to yield a specific design lift coefficient, so the hydrofoils should also be compared at a constant C_L . This comparison is shown on the right side of Figure 9 for $C_L = 0.75$. The CFRP hydrofoil with $\theta_f = -30^\circ$, requires the lowest angle of attack, while the $\theta_f = +30^\circ$ requires the highest. This is expected, given the nose-up and nose-down twist for the -30° and the $+30^\circ$ hydrofoils, respectively.

To achieve the same C_L , the CFRP hydrofoil with $\theta_f = -30^\circ$ effectively unloads the root to counter the higher loading at the tip. Therefore, the center of lift moves towards the tip for the hydrofoil with $\theta_f = -30^\circ$, which leads to a higher bending moment and also a higher induced drag. The opposite trend is observed for the CFRP hydrofoil with $\theta_f = +30^\circ$. The strength of the tip vortex is correlated to the pressure difference between suction side and pressure side at the tip, i.e., the tip loading. Therefore, the CFRP hydrofoil with $\theta_f = -30^\circ$ experiences the strongest tip vortex, while the hydrofoil with $\theta_f = +30^\circ$ has the weakest tip vortex, which is also suggested by the streamlines near the tip. Thus, at the same lift condition, the CFRP hydrofoil with $\theta_f = +30^\circ$ has a lower lift induced drag compared to the stainless steel hydrofoil due to the weaker tip vortex.

For rotating propeller blades, the tip experiences the highest velocity compared to other parts of blade at a given RPM as it is farthest from the shaft. Hence, the high local velocity at the tip makes it susceptible to tip vortex cavitation. If the effective angle of attack is high at the tip, the likelihood of tip vortex cavitation increases, which can in turn lead to flow-induced vibrations, noise, as well as blade surface erosion. Therefore, as shown in Figure 9, the CFRP hydrofoil with $\theta_f = -30^\circ$ is more susceptible to tip vortex cavitation compared to other two hydrofoils.

4.3 Force coefficients and deformation

To show the bend-twist coupling effects of the different materials on the steady-state hydroelastic performance, we show hydrostructural analysis results for the composite hydrofoils with different CFRP orientations for angles of attack ranging from 0° to 12° (Figure 10). Bending towards the suction side is defined as positive and nose-up twisting is defined as positive, as shown in Figure 9. Results for the tip bending are non-dimensionalized by half the mean chord, so it is shown as $2\delta_{\text{tip}}/c$.

The stainless steel hydrofoil is practically rigid, as made obvious by the negligible tip bending (δ_{tip}) and tip twisting (θ_{tip}) deformations. For the $\theta_f = 0^\circ$ hydrofoil, there is some coupling between upwards bending and nose-up twist. The material bend-twist coupling is zero, but there is flow-induced bend-twist coupling caused by the fact that the chordwise center of lift is upstream of the elastic axis. Based on the tip bending and twisting results shown in Figure 10, we can see that while all the hydrofoils undergo upwards bending due to lift, the hydrofoils with $\theta_f > 0^\circ$ undergo negative tip twist (nose-down), while those with negative θ_f experience positive tip twist (nose-up).

Changes in the curves of C_L and C_M from the initial linear line can be good in-

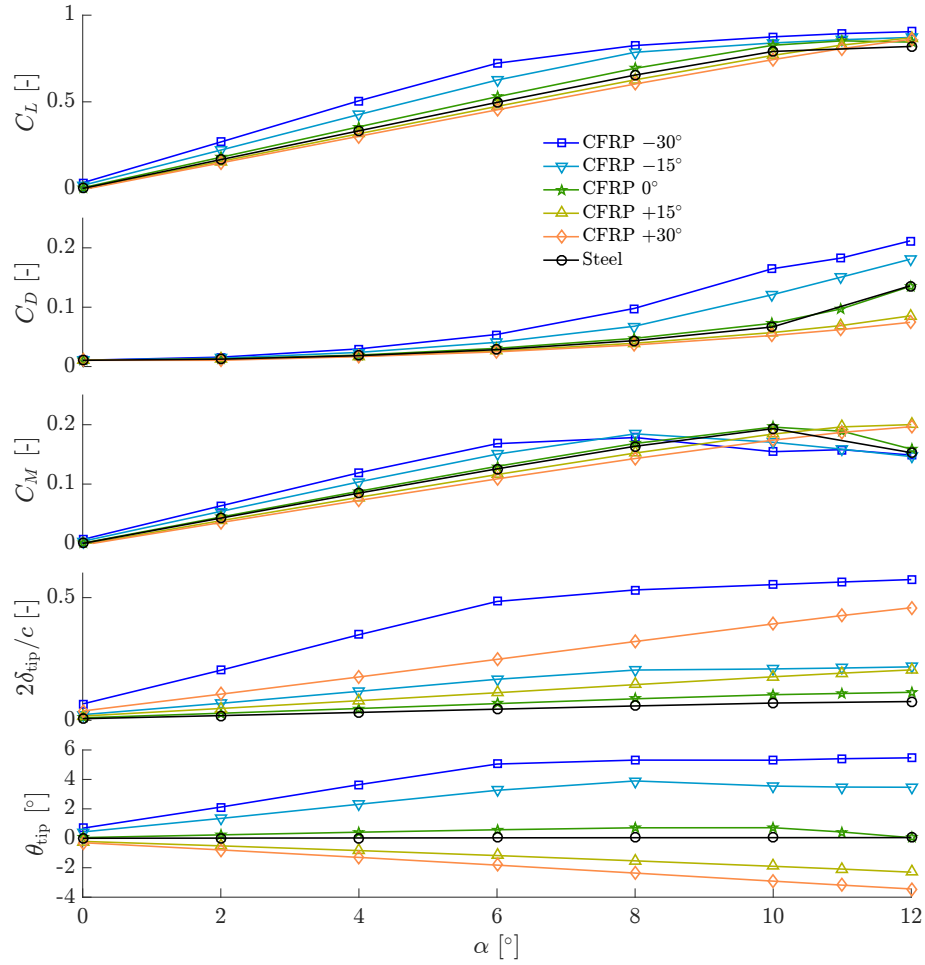


Figure 10: Hydrostructural simulation results of force coefficients and deformations for CFRP hydrofoils with different fiber orientations and the stainless steel hydrofoil. Negative θ_f hydrofoils see earlier reduction in lift and moment slope due to flow separation when compared to the positive θ_f and the stainless steel (rigid) hydrofoils.

dicators of flow separation and stall. When the slopes of the C_L and C_M versus α start to decrease, that is an indication that separation occurs. The decrease in C_L and C_M suggests stall. In Figure 10, the slopes of C_L and C_M curves in the pre-stall region decrease when the θ_f is increased from -30° to $+30^\circ$ because of the reduction in effective angle of attack caused by the nose-down twist. The results also show that the slopes of the C_L and C_M curves for the -30° hydrofoil deviate from the linear trend earlier than the other hydrofoils, suggesting earlier flow separation. The same trend is found in experimental results of Young et al. [15].

As shown in Figure 10, no lift stall is observed for all hydrofoils within the investigated α range, but pitch moment stall is observed for hydrofoils with $\theta_f \leq 0^\circ$ as shown by the decreases of C_M . Note that the C_M slope decays prior to the C_L slope because C_M depends on C_L and the distance between the center of pressure and the elastic axis. The center of pressure moves towards the midchord as flow separates on the suction side, leading to a rapid reduction in C_M . The separation for $\theta_f = -30^\circ$ happens at $\alpha = 6^\circ$, while for $\theta_f = -15^\circ$, the separation starts at $\alpha = 8^\circ$. No separation is observed below $\alpha = 12^\circ$ for the hydrofoils with $\theta_f > 0^\circ$ and the stainless steel hydrofoil, indicating delayed flow separation. This observation is consistent with the streamlines shown in Figure 9.

The drag coefficient, C_D , consists of three components: skin friction drag, form drag, and lift induced drag. Since the lift is higher for $\theta_f < 0^\circ$ at the same α , the lift induced drag increases for $\theta_f < 0^\circ$ and the form drag is higher because of the higher effective angle of attack, both leading to higher total drag. Notice that C_D increases substantially when flow separates, and hence much higher C_D is observed for the $\theta_f = -30^\circ$ hydrofoil for $\alpha > 6^\circ$.

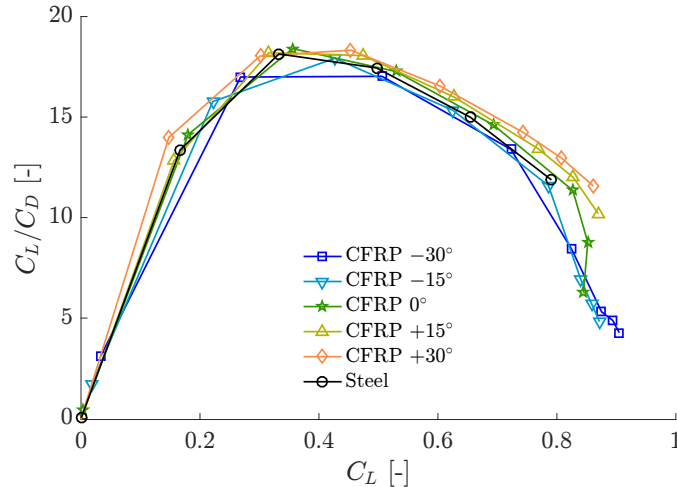


Figure 11: Hydrodynamic efficiency C_L/C_D versus C_L for various hydrofoils based on hydrostructural simulations.

As previously mentioned, the fair way to compare the drag or efficiency of different hydrofoils is to compare the performance at the same lift condition. Figure 11 compares the efficiency between different θ_f by plotting C_L/C_D versus C_L . The hydrofoils with

$\theta_f > 0^\circ$ have higher efficiency than $\theta_f < 0^\circ$. From Figure 11 we can see that the highest efficiency corresponds to $\theta_f = +30^\circ$, while the lowest efficiency corresponds to $\theta_f = -30^\circ$. The slopes and curvature of the streamlines in Figure 9 show that, at the same flow condition, the tip vortex for the stainless steel hydrofoil is stronger than that for the CFRP hydrofoil with $\theta_f = +30^\circ$, which is responsible for the lower efficiency for the stainless steel hydrofoil compared to the CFRP hydrofoil with $\theta_f = +30^\circ$.

4.4 Load-dependency

To illustrate the load dependency, we show hydrostructural analysis results of two different CFRP hydrofoils in Figure 12 under different loading conditions, with inflow velocity U ranging from 7.9 m/s to 11.4 m/s and α ranging from 0° to 12° . Note that the Reynolds number increases linearly with the inflow velocity.

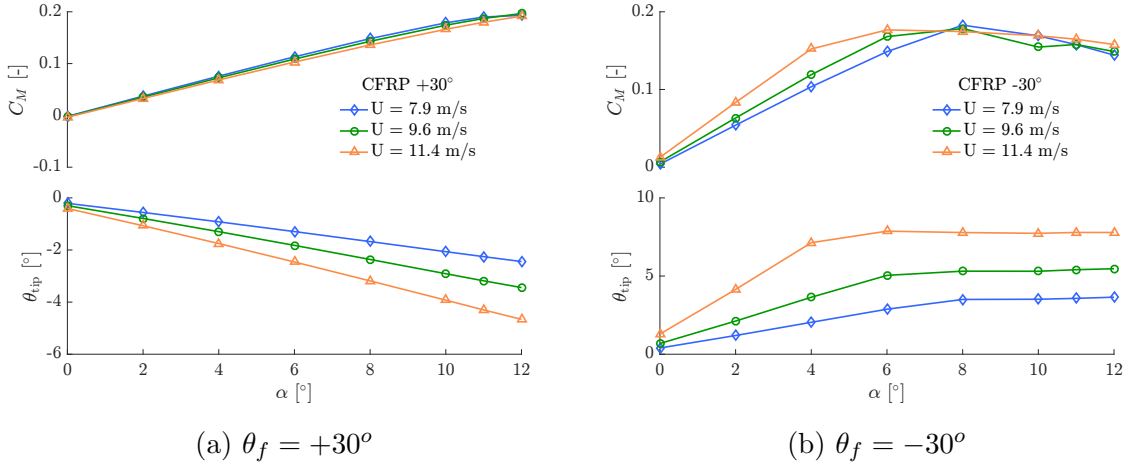


Figure 12: The load-dependency induced by bending-up and nose-down coupling effect for the $\theta_f = +30^\circ$ leads to decreasing moment coefficient with increasing inflow velocity, while the opposite trend is observed for the CFRP hydrofoil with $\theta_f = -30^\circ$. The velocity dependency is smaller for the CFRP hydrofoil with $\theta_f = +30^\circ$.

Different fiber orientations show distinct load-dependent effects. Increasing U reduces the resultant force coefficient because of the greater nose-down twist for the CFRP hydrofoil with $\theta_f = +30^\circ$, while the opposite trend is observed for the CFRP hydrofoil with $\theta_f = -30^\circ$. For the CFRP hydrofoil with $\theta_f = -30^\circ$, the bending-up and nose-up bend-twist coupling acts to increase the effective angle of attack together with the flow-induced nose-up twist, resulting in higher lift and moment coefficients with higher U . As a result, the CFRP hydrofoil with $\theta_f = -30^\circ$ is more susceptible to flow separation and static divergence. In contrast, for the $+30^\circ$ hydrofoil, the nose-down twist induced by material bend-twist coupling is greater than the nose-up twist induced by the flow, and hence the net tip twist observed in Figure 12a is negative. The opposite direction of twist induced by the flow and material is responsible for the smaller U dependency for the $\theta_f = +30^\circ$ hydrofoil compared to the $\theta_f = -30^\circ$ hydrofoil. In addition, since the increased load induced by higher U is offset by the

decreased effective angle of attack for the CFRP hydrofoil with $\theta_f = +30^\circ$, it is not susceptible to static divergence for nominal inflow.

4.5 Susceptibility to static divergence

Static divergence occurs when the fluid disturbing moment is equal to or exceeds the structural elastic restoring moment, at which point the deformations theoretically goes to infinity. However, in practice material failure occurs before static divergence. Nevertheless, it is critical to predict the static divergence speed to avoid material failure or excessive deformation.

Following Fung [47], Liu and Young [26] introduced a linear relationship between $\alpha/\theta_{\text{tip}}$ and $1/q$ using a theoretical model given by

$$\frac{\alpha}{\theta_{\text{tip}}} = q_D \left(\frac{1}{q} - \frac{1}{q_D} \right), \quad (1)$$

where $q = 1/2\rho_f U^2$ is the dynamic pressure, and $q_D = 1/2\rho_f U_D^2$ is the critical static divergence dynamic pressure.

However, they did not consider the spanwise variation of the twist. To consider the spanwise twist distribution, we incorporate a factor that relates the 3D spanwise twist distribution to the 2D twist. To derive this factor, we approximate the non-dimensional spanwise twist shape function ($\bar{\theta} = \theta/\theta_{\text{tip}}$) as

$$\bar{\theta}(\bar{y}) = \frac{1}{2} + \frac{1}{2} \sin \left(\pi \bar{y} - \frac{\pi}{2} \right), \quad (2)$$

where $\bar{y} = y/b$ is the non-dimensionalized spanwise location. This approximation was obtained by considering the boundary conditions, $\bar{\theta}(0) = 0$, $\bar{\theta}'(0) = 0$, $\bar{\theta}'(1) = 0$. The comparison between the assumed twist distribution $\bar{\theta}(\bar{y})$ and the numerical results are shown in Appendix C. Integration of the twist shape function $\bar{\theta}$, from $\bar{y} = 0$ to $\bar{y} = 1$, yields a factor of 0.5. Therefore, the Equation (1) becomes

$$\frac{\alpha}{0.5\theta_{\text{tip}}} = q_D \left(\frac{1}{q} - \frac{1}{q_D} \right). \quad (3)$$

The detailed derivation considering the spanwise dependence is shown in Young et al.[15], where they used $2/\pi$ as the factor. When the inflow velocity U approaches the critical divergence speed U_D , $q = q_D$ and $\alpha/0.5\theta_{\text{tip}} \rightarrow 0$, which implies $\theta_{\text{tip}} \rightarrow \infty$. To study the susceptibility to static divergence, we use the hydrostructural simulation results to fit the linear relationship to find the critical divergence dynamic pressure, as shown in Figure 13.

The predicted critical divergence dynamic pressures and calculated divergence speeds are summarized in Table 7. At nominal inflow conditions, orienting fibers towards the trailing edge ($\theta_f < 0^\circ$) accelerates susceptibility to divergence due to the increasing effective angle of attack with higher loads [15]. This prediction is consistent with the discussions in Sections 4.2 and 4.3. When the fibers are oriented towards the leading

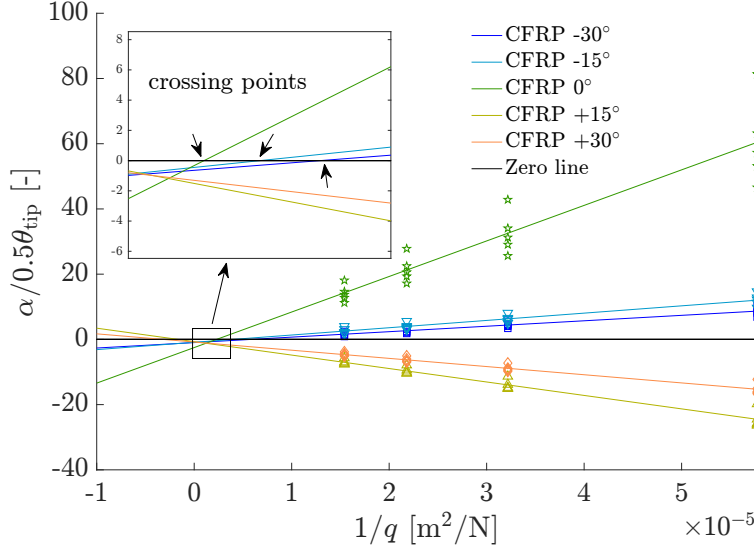


Figure 13: $\alpha/0.5\theta_{tip}$ versus $1/q$ for a range of flow conditions. For positive angle of attack α , sweeping the fiber orientation backward increases the susceptibility to divergence for nominal inflow conditions.

edge ($\theta_f > 0^\circ$), the divergence dynamic pressures are non-existent (negative), which indicates the foil is not susceptible to static divergence at the nominal inflow conditions. However, divergence is still possible for reverse inflow, which can occur for propellers in the crash back condition and tidal turbines during tidal reversal [15].

Table 7: Predicted divergence speeds for composite hydrofoils.

θ_f [°]	-30°	-15°	0°	+15°	+30°
q_D [N/m ²]	1.7×10^5	2.4×10^5	4.3×10^5	-6×10^5	-3.1×10^5
U_D [m/s]	18.5	22.4	29.5	-	-

4.6 Failure index contour

Since realistic composite structures have complex layouts and require complicated manufacturing techniques, it is hard to perform failure analysis on composite structures. There exist many different material failure mechanisms for composite structures, which require appropriate mechanistic material failure prediction models [48]. Here, we use the tensile/compressive matrix cracking criterion proposed by Hashin [49] and the delamination in tension/compression criterion proposed by Ye [50] to evaluate the failure susceptibility and locate the region of failure.

The matrix tensile/compressive cracking failure is defined as,

$$I_M = \left(\frac{\sigma_{11}}{X_T}\right)^2 + \left(\frac{\sigma_{12}}{S_{12}}\right)^2 + \left(\frac{\sigma_{23}}{S_{23}}\right)^2, \text{ when } \sigma_{11} > 0 \quad (4)$$

$$I_M = \left(\frac{\sigma_{11}}{X_C}\right)^2 + \left(\frac{\sigma_{12}}{S_{12}}\right)^2 + \left(\frac{\sigma_{23}}{S_{23}}\right)^2, \text{ when } \sigma_{11} < 0 \quad (5)$$

while the delamination in tension/compression is defined as,

$$I_D = \left(\frac{\sigma_{33}}{Z_T}\right)^2 + \left(\frac{\sigma_{13}}{S_{13}}\right)^2 + \left(\frac{\sigma_{23}}{S_{23}}\right)^2, \text{ when } \sigma_{33} > 0 \quad (6)$$

$$I_D = \left(\frac{\sigma_{33}}{Z_C}\right)^2 + \left(\frac{\sigma_{13}}{S_{13}}\right)^2 + \left(\frac{\sigma_{23}}{S_{23}}\right)^2, \text{ when } \sigma_{33} < 0 \quad (7)$$

where $\{\sigma\}_{ij} = [\sigma_{11}, \sigma_{22}, \sigma_{33}, \sigma_{23}, \sigma_{13}, \sigma_{12}]^T$ represents stress components in the local material coordinates shown in Figure 1. X_T/X_C is the transverse tensile/compressive strength in 1-direction shown in Figure 1. Z_T/Z_C is the transverse tensile/compressive strength in 3-direction. S_{ij} represent the shear strengths.

Figure 14 shows the matrix tensile/compressive cracking failure index I_{MT} and delamination in tension/compression index I_D for the CFRP hydrofoils with $\theta_f = -30^\circ$ and $\theta_f = +30^\circ$ at $C_L = 0.75$. Since the material failure is most likely to happen in tension, the failure index contours on the pressure sides are shown. For both hydrofoils, there are large areas that I_M exceeds the critical failure value 1, which suggests the occurrence of material failure. However, since we only model a single CFRP layer and this material layup is hardly used in a structure manufacturing, the stress is not representative for a real design and thus the failure criteria index values are not realistic here. When subject to loads that are not along the principal axis, the single layer of CFRP can easily fail due to its anisotropic properties. In addition, the use of the fixed boundary condition induces a significant stress concentration at the root without proper fillets. Nevertheless, we can still see from the failure contours in Figure 14 that the two CFRP hydrofoils have different failure locations. The bending-up and nose-up bend-twist coupling causes higher combined stress near the leading edge at the root for the CFRP hydrofoil with $\theta_f = -30^\circ$. The bending-up and nose-down bend-twist coupling causes higher combined stress near the trailing edge at the root for the CFRP hydrofoil with $\theta_f = 30^\circ$, as shown in Figure 14.

5 Conclusions

The objectives of this work are to develop and verify the composite finite-element implementation in a high-fidelity hydrostructural solver and to improve the understanding of load-dependent bend-twist coupling effects on the hydroelastic performance of composite hydrofoils in viscous flow through numerical simulations. We extended a previous developed MACH framework to simulate the performance of composite hydrodynamic lifting surfaces by adding orthotropic solid elements in the FEM solver TACS. The verification study showed good agreement between predictions from TACS and the commercial FEM solver ABAQUS. By coupling TACS with a RANS solver, MACH is able to capture viscous fluid-structure interaction response, including flow separation and the tip vortex, as well as the susceptibility to structural failure. The model used

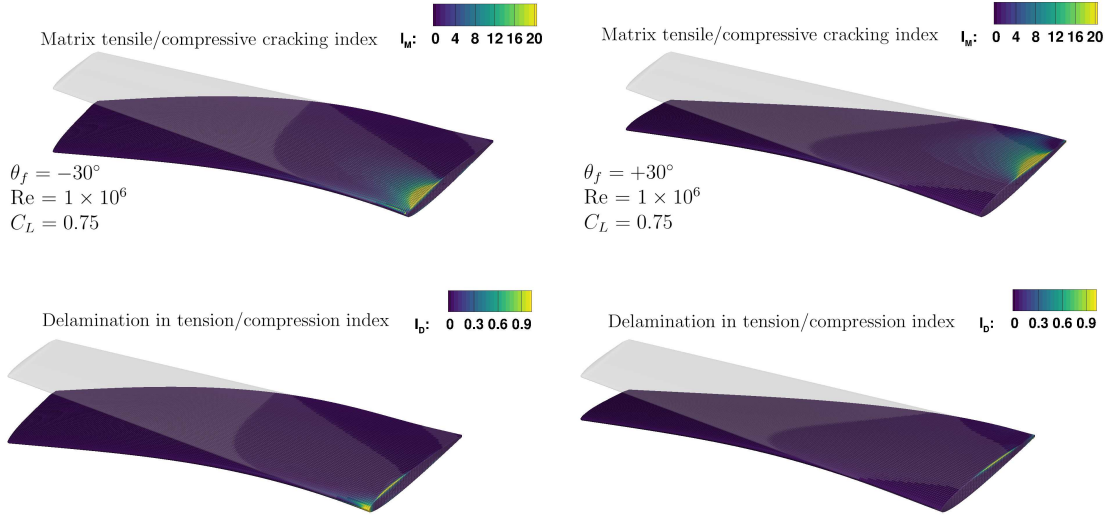


Figure 14: Matrix tensile/compressive cracking failure index and delamination in tension/compression failure index contours on the pressure sides for the unidirectional CFRP hydrofoils with $\theta_f = -30^\circ$ and $\theta_f = 30^\circ$. The deformations are multiplied by a factor of two to make them more apparent.

for simulation in this work was a cantilevered hydrofoil with a modified NACA 0009 cross section and a linearly tapered planform with no sweep.

We first studied the influence of fiber orientation on the free vibration response. We showed by modal analysis that changing the fiber orientation of the CFRP layer altered the mode shapes and the natural frequencies of the hydrofoils, which was caused by the change in the bending stiffness, torsional stiffness, and bend-twist coupling. The first modes for all fiber orientations were bending-dominated, because of the high aspect ratio. The second modes were twist-dominated when the fibers were oriented along the spanwise axis, but were changed to bending-dominated when the fibers were oriented away from the spanwise axis (either forward or backward). This change in the second mode was due to the decrease in bending rigidity. The changes in the mode shapes further complicate their effect on the added mass, which depends on the displacement direction in addition to the fluid density. As demonstrated by the modal analysis of a composite cantilevered plate, the in-water natural frequencies are much lower than the in-air natural frequencies because of the fluid added mass effect. Therefore, it is important to consider the influence of fiber orientation on the modal characteristics and resulting change in natural frequencies to avoid resonant vibration issues.

We then performed hydrostructural simulations for hydrofoils with different fiber orientations to investigate how the fiber orientation affected the steady-state hydroelastic response and thus efficiency, divergence boundary, and structural failure. The results show that hydrofoils with fibers oriented toward the foil leading edge resulted in bend-twist coupling with a nose-down deformation, which led to lower hydrodynamic load coefficients with increasing flow speed. The opposite trend was observed for fibers oriented toward the foil trailing edge, which resulted in nose-up deformation.

In addition, orienting the fibers towards the leading edge attenuated the tip vortex and delayed flow separation by reducing the effective angle of attack at the tip, which led to a higher efficiency. The reduced effective angle of attack also correlated with delayed separation and stall. The comparison of force coefficients showed that the hydrofoils with fiber oriented towards the leading edge delayed the reduction in the C_M - α slope. Reductions in the slope of C_L and C_M versus α indicate the onset of flow separation. Of the two, C_M is more sensitive to separation, as it is dependent on both C_L and the center of pressure.

We also compared the load-dependencies of two hydrofoils with opposite fiber orientations to show the difference in the responses to increasing inflow velocity. Increasing the inflow velocity caused more nose-down twist for the hydrofoils with fiber oriented towards the leading edge. As a result, the effective angle of attack was further decreased to offset the effect of increasing inflow velocity. On the other hand, for the hydrofoils with fibers oriented towards the trailing edge, the effective angle of attack kept increasing with higher inflow velocity, making it more susceptible to flow separation, stall, and static divergence. We predicted the divergence speed by extrapolating the static hydrostructural simulation results. The prediction showed that the critical divergence speeds for hydrofoils with fibers oriented towards the trailing edge are much lower than the hydrofoil with fiber aligned with spanwise axis ($\theta_f = 0^\circ$), and the hydrofoils with fibers oriented towards the leading edge are not susceptible to divergence considering the nominal inflow direction. Finally, we showed the comparison of material matrix tensile/compressive cracking and delamination in tension/compression index contours. The fiber orientation affected the failure location.

This paper showed that our aerostructural analysis framework is able to predict the steady-state hydroelastic response of composite hydrofoils in viscous flow. This framework can be used for design optimization of composite hydrodynamic lifting surfaces in the future. Adding the properties of composite materials as design variables, such as the fiber orientation, helps to modify the dynamic characteristics and further improve the efficiencies of hydrodynamic lifting surfaces, and avoid different failure modes. The analysis results presented in this work will also guide future design optimization problems. As for the limitation on the failure prediction, we plan to consider more thorough materials properties and composite layups, and improve the modeling of the boundary condition in the future to yield more accurate stresses and failure indices.

6 Acknowledgments

Support for this research was provided by the U.S. Office of Naval Research (Contract N00014-16-1-2972 and N00014-18-1-2333), managed by Ms. Kelly Cooper.

Appendix A Constitutive Equations

The final constitutive equations for orthotropic elements in global coordinates are written as,

$$\begin{bmatrix} \sigma_{xx} \\ \sigma_{yy} \\ \sigma_{zz} \\ \sigma_{yz} \\ \sigma_{xz} \\ \sigma_{xy} \end{bmatrix} = \begin{bmatrix} \bar{C}_{11} & \bar{C}_{12} & \bar{C}_{13} & 0 & 0 & \bar{C}_{16} \\ \bar{C}_{12} & \bar{C}_{22} & \bar{C}_{23} & 0 & 0 & \bar{C}_{26} \\ \bar{C}_{13} & \bar{C}_{23} & \bar{C}_{33} & 0 & 0 & \bar{C}_{36} \\ 0 & 0 & 0 & \bar{C}_{44} & \bar{C}_{45} & 0 \\ 0 & 0 & 0 & \bar{C}_{45} & \bar{C}_{55} & 0 \\ \bar{C}_{16} & \bar{C}_{26} & \bar{C}_{36} & 0 & 0 & \bar{C}_{66} \end{bmatrix} \begin{bmatrix} \epsilon_{xx} \\ \epsilon_{yy} \\ \epsilon_{zz} \\ \epsilon_{yz} \\ \epsilon_{xz} \\ \epsilon_{xy} \end{bmatrix} \quad (1)$$

Using the fiber orientation (θ_f) defined relative to the y -axis, which is defined as positive when pointing towards the leading edge, the individual components of the $[\bar{C}]$ can be described as,

$$\begin{aligned} \bar{C}_{11} &= m^4 C_{11} + 2m^2 n^2 (C_{12} + 2C_{66}) + n^4 C_{22} \\ \bar{C}_{12} &= n^2 m^2 (C_{11} + C_{22} - 4C_{66}) + (n^4 + m^4) C_{12} \\ \bar{C}_{13} &= m^2 C_{13} + n^2 C_{23} \\ \bar{C}_{16} &= nm [m^2 (C_{11} - C_{12} - 2C_{66}) + n^2 (C_{12} - C_{22} + 2C_{66})] \\ \bar{C}_{22} &= n^4 C_{11} + 2m^2 n^2 (C_{12} + 2C_{66}) + m^4 C_{22} \\ \bar{C}_{23} &= n^2 C_{13} + m^2 C_{23} \\ \bar{C}_{26} &= nm [n^2 (C_{11} - C_{12} - 2C_{66}) + m^2 (C_{12} - C_{22} + 2C_{66})] \\ \bar{C}_{33} &= C_{33} \\ \bar{C}_{36} &= mn (C_{13} - C_{23}) \\ \bar{C}_{44} &= m^2 C_{44} + n^2 C_{55} \\ \bar{C}_{45} &= mn (C_{55} - C_{44}) \\ \bar{C}_{55} &= n^2 C_{44} + m^2 C_{55} \\ \bar{C}_{66} &= n^2 m^2 (C_{11} - 2C_{12} + C_{22}) + (n^2 - m^2)^2 C_{66}, \end{aligned} \quad (2)$$

where $m = \cos\theta_f$, $n = \sin\theta_f$, θ_f is the fiber orientation angle in radians. The angle θ_f is the angle between the fiber orientation and y -axis, as shown in Figure 1. The original

stiffness components $\{C\}_{ij}$ are,

$$\begin{aligned}
C_{11} &= \frac{1 - \nu_{23}\nu_{32}}{E_2 E_3 D} \\
C_{12} &= \frac{\nu_{21} + \nu_{23}\nu_{31}}{E_2 E_3 D} \\
C_{13} &= \frac{\nu_{31} + \nu_{21}\nu_{32}}{E_2 E_3 D} \\
C_{22} &= \frac{1 - \nu_{13}\nu_{31}}{E_2 E_3 D} \\
C_{23} &= \frac{\nu_{32} + \nu_{12}\nu_{31}}{E_1 E_3 D} \\
C_{33} &= \frac{1 - \nu_{12}\nu_{21}}{E_1 E_2 D} \\
C_{44} &= G_{23} \\
C_{55} &= G_{13} \\
C_{66} &= G_{12} \\
D &= \frac{1 - \nu_{12}\nu_{21} - \nu_{23}\nu_{32} - \nu_{13}\nu_{31} - 2\nu_{21}\nu_{32}\nu_{13}}{E_1 E_2 E_3},
\end{aligned} \tag{3}$$

where E_1 , E_2 , and E_3 are the Young's moduli in 1, 2, and 3 directions, respectively, G_{ij} represents the shear modulus, and ν_{ij} are the Poisson's ratios.

Appendix B Mode Shapes of Composite Hydrofoils predicted using ABAQUS

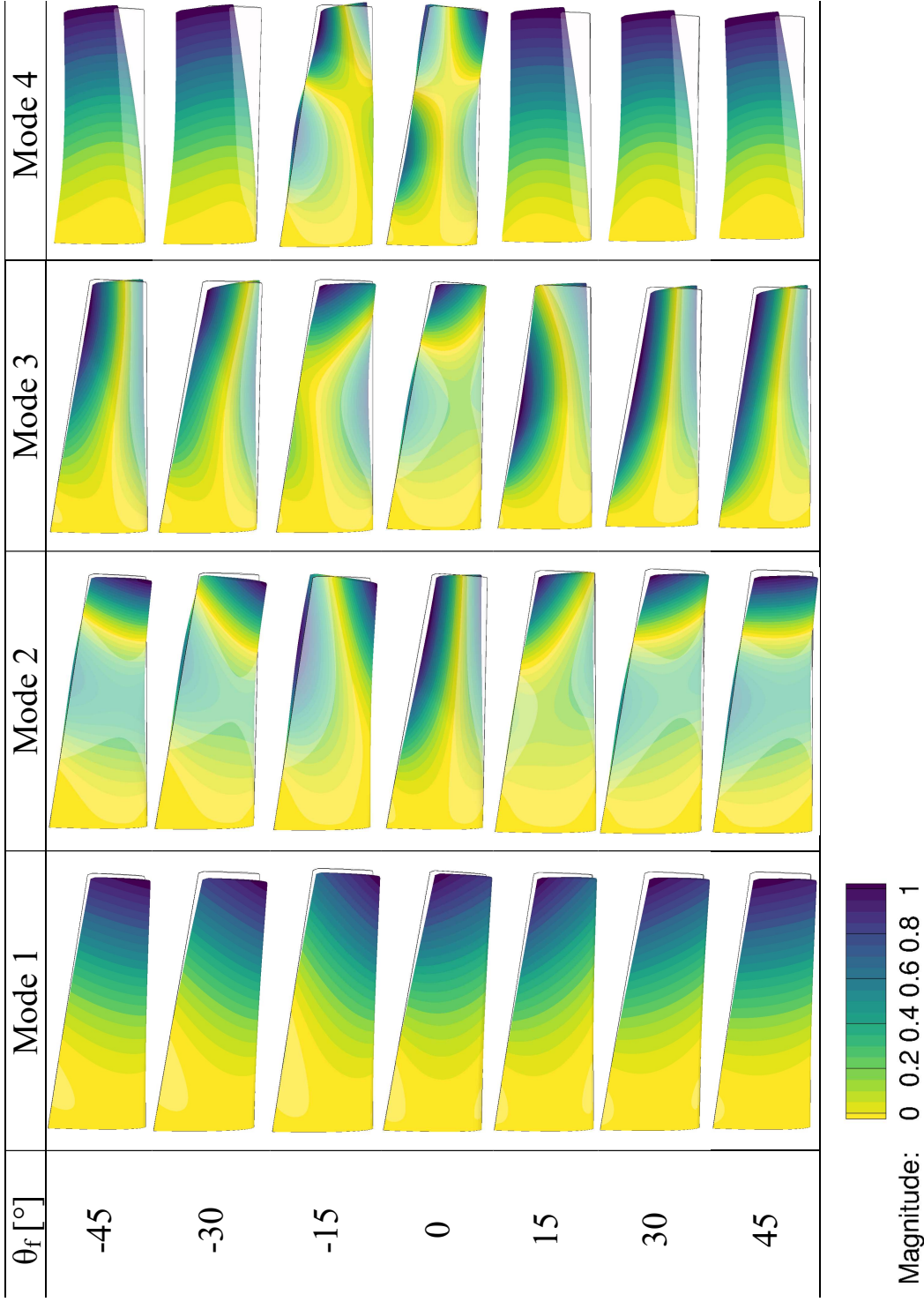


Figure B.1: The first four predicted in-air mode shapes of a cantilevered foil for a range of θ_f obtained using ABAQUS. The contours represent the scaled displacement amplitude. Note that the contour legend only shows a normalized range and does not imply the actual displacement magnitude. The predicted mode shapes using ABAQUS agree well with those obtained using TACS, which are shown in 8. Note the good agreement between the mode shapes predicted using the two structural solvers.

Appendix C Normalized Spanwise Twist Distribution

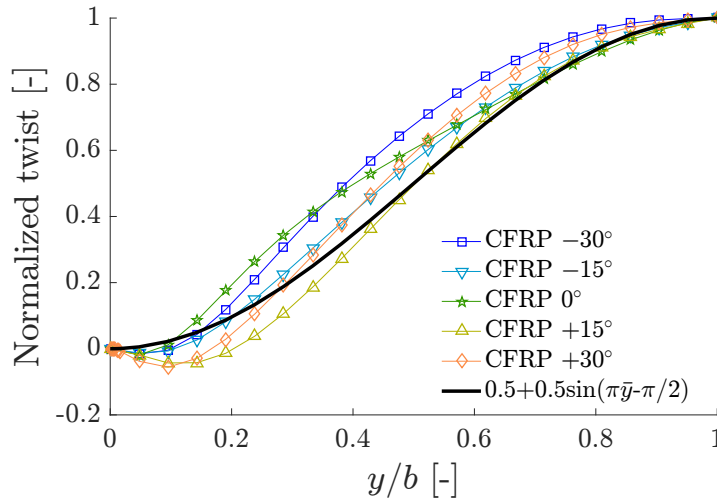


Figure C.1: Normalized spanwise twist distribution for five CFRP hydrofoils compared to the approximation given by Equation 2.

References

- [1] UNCTAD, *Review of Maritime Transport 2016*, UNCTAD, UNCTAD/RMT/2016, 2016.
- [2] Faber, J., Hoen, M., Koopman, M., Nelissen, D., and Ahdour, S., “Estimated Index Values of New Ships,” *CE Delft Technical Report*, 2015.
- [3] Peri, D., Rossetti, M., and Campana, E. F., “Design optimization of ship hulls via CFD techniques,” *Journal of Ship Research*, Vol. 45, No. 2, 2001, pp. 140–149.
- [4] Peri, D., and Campana, E. F., “Multidisciplinary Design Optimization of a Naval Surface Combatant,” *Journal of Ship Research*, Vol. 47, No. 1, 2003, pp. 1–12.
- [5] Campana, E. F., Peri, D., Tahara, Y., and Stern, F., “Shape optimization in ship hydrodynamics using computational fluid dynamics,” *Computer Methods in Applied Mechanics and Engineering*, Vol. 196, No. 1, 2006, pp. 634–651.
- [6] Tahara, Y., Tohyama, S., and Katsui, T., “CFD-based multi-objective optimization method for ship design,” *International Journal for Numerical Methods in Fluids*, Vol. 52, No. 5, 2006, pp. 499–527.
- [7] Lee, Y., and Lin, C., “Optimized design of composite propeller,” *Mechanics of advanced materials and structures*, Vol. 11, No. 1, 2004, pp. 17–30.

- [8] Blasques, J. P., Berggreen, C., and Andersen, P., “Hydro-elastic analysis and optimization of a composite marine propeller,” *Marine Structures*, Vol. 23, No. 1, 2010, pp. 22–38.
- [9] Young, Y. L., Motley, M. R., Barber, R., Chae, E. J., and Garg, N., “Adaptive Composite Marine Propulsors and Turbines: Progress and Challenges,” *Applied Mechanics Reviews*, Vol. 68, No. 6, 2016, p. 060803.
- [10] Liu, Z., and Young, Y. L., “Utilization of bend–twist coupling for performance enhancement of composite marine propellers,” *Journal of Fluids and Structures*, Vol. 25, No. 6, 2009, pp. 1102–1116.
- [11] Motley, M., Liu, Z., and Young, Y., “Utilizing fluid–structure interactions to improve energy efficiency of composite marine propellers in spatially varying wake,” *Composite Structures*, Vol. 90, No. 3, 2009, pp. 304–313.
- [12] Nelson, M., Temple, D., Hwang, J. T., Young, Y. L., Martins, J. R. R. A., and Collette, M., “Simultaneous Optimization of Propeller-Hull Systems to Minimize Lifetime Fuel Consumption,” *Applied Ocean Research*, Vol. 43, 2013, pp. 46–52. doi:10.1016/j.apor.2013.07.004.
- [13] Kramer, M. R., Motley, M. R., and Young, Y. L., “An Integrated Probability-Based Propulsor-Hull Matching Methodology,” *Journal of Offshore Mechanics and Arctic Engineering*, Vol. 135, No. 1, 2013, p. 011801.
- [14] Mouritz, A., Gellert, E., Burchill, P., and Challis, K., “Review of advanced composite structures for naval ships and submarines,” *Composite structures*, Vol. 53, No. 1, 2001, pp. 21–42.
- [15] Young, Y. L., Garg, N., Brandner, P. A., Pearce, B. W., Butler, D., Clarke, D., and Phillips, A. W., “Load-Dependent Bend-Twist Coupling Effects on the Steady-state Hydroelastic Response of Composite Hydrofoils,” *Composite Structures*, Vol. 189, No. 1, 2018, pp. 398–418. doi:10.1016/j.compstruct.2017.09.112.
- [16] Mallick, P., *Fiber-Reinforced Composites: Materials, Manufacturing, and Design*, 3rd ed., CRC Press, 2007.
- [17] Soutis, C., “Fibre reinforced composites in aircraft construction,” *Progress in Aerospace Sciences*, Vol. 41, 2005, pp. 143–151.
- [18] Guo, S., Cheng, W., and Cui, D., “Aeroelastic Tailoring of Composite Wing Structures by Laminate Layup Optimization,” *AIAA Journal*, 2006, p. 3146–3150. doi:10.2514/1.20166.
- [19] Brooks, T. R., Kennedy, G. J., and Martins, J. R. R. A., “High-fidelity Multipoint Aerostructural Optimization of a High Aspect Ratio Tow-steered Composite Wing,” *Proceedings of the 58th AIAA/ASCE/AHS/ASC Structures, Structural Dynamics, and Materials Conference, AIAA SciTech Forum*, Grapevine, TX, 2017. doi:10.2514/6.2017-1350.

- [20] Hayat, K., and Ha, S. K., “Load mitigation of wind turbine blade by aeroelastic tailoring via unbalanced laminates composites,” *Composite Structures*, Vol. 128, 2015, pp. 122–133.
- [21] Kramer, M. R., Liu, Z., and Young, Y. L., “Free vibration of cantilevered composite plates in air and in water,” *Composite Structures*, Vol. 95, 2013, pp. 254–263.
- [22] Berthelot, J.-M., Assarar, M., Sefrani, Y., and Mahi, A. E., “Damping analysis of composite materials and structures,” *Composite Structures*, Vol. 85, No. 3, 2008, pp. 189–204.
- [23] Lee, H., Song, M.-C., Han, S., Chang, B.-J., and Suh, J.-C., “Hydro-elastic aspects of a composite marine propeller in accordance with ply lamination methods,” *Journal of Marine Science and Technology*, Vol. 22, No. 3, 2017, pp. 479–493.
- [24] Lin, G.-F., “Comparative Stress/Deflection Analyses of a Thick-Shell Composite Propeller Blade,” Tech. rep., DTRC, December 1991.
- [25] Motley, M. R., and Young, Y. L., “Performance-based design and analysis of flexible composite propulsors,” *Journal of Fluids and Structures*, Vol. 27, No. 8, 2011, pp. 1310–1325.
- [26] Liu, Z., and Young, Y. L., “Static divergence of self-twisting composite rotors,” *Journal of Fluids and Structures*, Vol. 26, No. 5, 2010, pp. 841–847.
- [27] Young, Y. L., “Fluid–structure interaction analysis of flexible composite marine propellers,” *Journal of Fluids and Structures*, Vol. 24, No. 6, 2008, pp. 799–818.
- [28] Pluciński, M. M., Young, Y. L., and Liu, Z., “Optimization of a self-twisting composite marine propeller using Genetic algorithms,” *16th International conference on composite materials, Kyoto, Japan (2007)*, 2007.
- [29] Gowing, S., Coffin, P., and Dai, C., “Hydrofoil cavitation improvements with elastically coupled composite materials,” *Proceedings of the 25th American Towing Tank Conference*, 1998.
- [30] Garg, N., Kenway, G. K. W., Martins, J. R. R. A., and Young, Y. L., “High-fidelity Multipoint Hydrostructural Optimization of a 3-D Hydrofoil,” *Journal of Fluids and Structures*, Vol. 71, 2017, pp. 15–39. doi:10.1016/j.jfluidstructs.2017.02.001.
- [31] Kenway, G. K. W., and Martins, J. R. R. A., “Multipoint High-Fidelity Aerostructural Optimization of a Transport Aircraft Configuration,” *Journal of Aircraft*, Vol. 51, No. 1, 2014, pp. 144–160. doi:10.2514/1.C032150.
- [32] Kenway, G. K. W., Kennedy, G. J., and Martins, J. R. R. A., “Scalable Parallel Approach for High-Fidelity Steady-State Aeroelastic Analysis and Derivative Computations,” *AIAA Journal*, Vol. 52, No. 5, 2014, pp. 935–951. doi:10.2514/1.J052255.

- [33] Garg, N., Pearce, B. W., Brandner, P. A., Phillips, A. W., Martins, J. R. R. A., and Young, Y. L., “Experimental Investigation of a Hydrofoil Designed via Hydrostructural Optimization,” *Journal of Fluids and Structures*, 2018.
- [34] Brooks, T. R., and Martins, J. R. R. A., “On Manufacturing Constraints for Tow-steered Composite Design Optimization,” *Composite Structures*, Vol. 204, 2018, pp. 548–559. doi:10.1016/j.compstruct.2018.07.100.
- [35] Kenway, G. K., Kennedy, G. J., and Martins, J. R. R. A., “A CAD-Free Approach to High-Fidelity Aerostructural Optimization,” *Proceedings of the 13th AIAA/ISSMO Multidisciplinary Analysis Optimization Conference*, Fort Worth, TX, 2010. doi:10.2514/6.2010-9231.
- [36] Mader, C. A., Martins, J. R. R. A., Alonso, J. J., and van der Weide, E., “ADjoint: An Approach for the Rapid Development of Discrete Adjoint Solvers,” *AIAA Journal*, Vol. 46, No. 4, 2008, pp. 863–873. doi:10.2514/1.29123.
- [37] Lyu, Z., Kenway, G. K., Paige, C., and Martins, J. R. R. A., “Automatic Differentiation Adjoint of the Reynolds-Averaged Navier–Stokes Equations with a Turbulence Model,” *21st AIAA Computational Fluid Dynamics Conference*, San Diego, CA, 2013. doi:10.2514/6.2013-2581.
- [38] Spalart, P., and Allmaras, S., “A One-Equation Turbulence Model for Aerodynamic Flows,” *30th Aerospace Sciences Meeting and Exhibit*, 1992. doi:10.2514/6.1992-439.
- [39] Kennedy, G. J., and Martins, J. R. R. A., “A parallel aerostructural optimization framework for aircraft design studies,” *Structural and Multidisciplinary Optimization*, Vol. 50, No. 6, 2014, pp. 1079–1101. doi:10.1007/s00158-014-1108-9.
- [40] structures, FEM, Nastran, *MSC.Nastran Reference Manual*, MSC Software Corp., 2001.
- [41] Brown, S. A., “Displacement Extrapolation for CFD+CSM Aeroelastic Analysis,” *Proceedings of the 35th AIAA Aerospace Sciences Meeting*, Reno, NV, 1997. AIAA 1997-1090.
- [42] Uyttersprot, L., “Inverse Distance Weighting Mesh Deformation,” Ph.D. thesis, Delft University of Technology, 2014.
- [43] Garg, N., Kenway, G. K. W., Lyu, Z., Martins, J. R. R. A., and Young, Y. L., “High-fidelity Hydrodynamic Shape Optimization of a 3-D Hydrofoil,” *Journal of Ship Research*, Vol. 59, No. 4, 2015, pp. 209–226. doi:10.5957/JOSR.59.4.150046.
- [44] Motley, M. R., Kramer, M. R., and Young, Y. L., “Free surface and solid boundary effects on the free vibration of cantilevered composite plates,” *Composite Structures*, Vol. 96, 2013, pp. 365–375.

- [45] Phillips, A., Cairns, R., Davis, C., Norman, P., Brandner, P., Pearce, B., and Young, Y. L., “Effect of material design parameters on the forced vibration response of composite hydrofoils in air and in water,” *Fifth International Symposium on Marine Propulsors, At Espoo, Finland*, 2017.
- [46] Zarruk, G., Brandner, P., Pearce, B., and Phillips, A. W., “Experimental study of the steady fluid-structure interaction of flexible hydrofoils,” *Journal of Fluids and Structure*, Vol. 51, 2014, pp. 326–343.
- [47] Fung, Y. C., *An Introduction to the Theory of Aeroelasticity*, Dover, 1994.
- [48] Papanikos, P., Tserpes, K. I., and Pantelakis, S., “Modelling of fatigue damage progression and life of CFRP laminates,” *Fatigue & Fracture of Engineering Materials & Structures*, Vol. 26, No. 1, 2003, pp. 37–47.
- [49] Hashin, Z., “Failure Criteria for Unidirectional Fiber Composites,” *Journal of Applied Mechanics*, Vol. 47, No. 2, 1980, pp. 329–334.
- [50] Ye, L., “Role of matrix resin in delamination onset and growth in composite laminates,” *Composites Science and Technology*, Vol. 33, No. 4, 1988, pp. 257 – 277.